JGR Solid Earth

RESEARCH ARTICLE
10.1029/2022JB024556

Low Thermal Conductivity of Hydrous Phase D Leads to a Self-Preservation Effect Within a Subducting Slab

HPSTAR 1432-2022

Wen-Pin Hsieh[1,2], Enrico Marzotto[3], Takayuki Ishii[4], Leonid Dubrovinsky[3], Alena A. Aslandukova[3], Giacomo Criniti[3], Yi-Chi Tsao[1], Chun-Hung Lin[1], Jun Tsuchiya[5], and Eiji Ohtani[6]

[1]Institute of Earth Sciences, Academia Sinica, Taipei, Taiwan, [2]Department of Geosciences, National Taiwan University, Taipei, Taiwan, [3]Bayerisches Geoinstitut, University of Bayreuth, Bayreuth, Germany, [4]Center for High Pressure Science and Technology Advanced Research, Beijing, China, [5]Geodynamics Research Center, Ehime University, Matsuyama, Japan, [6]Department of Earth Science, Graduate School of Science, Tohoku University, Sendai, Japan

Key Points:

- We precisely measured the thermal conductivity of Al- and (Al,Fe)-phase D at high pressure and wide range of temperature
- Thermal conductivity of (Al,Fe)-phase D is relatively low, except across the spin transition where it suddenly peaks and varies by four folds
- Low thermal conductivity of hydrous minerals maintains cold temperatures in a sinking slab, deepening the stability fields of slab minerals

Supporting Information:

Supporting Information may be found in the online version of this article.

Correspondence to:

W.-P. Hsieh and E. Ohtani,
wphsieh@earth.sinica.edu.tw;
eohtani@tohoku.ac.jp

Citation:

Hsieh, W.-P., Marzotto, E., Ishii, T., Dubrovinsky, L., Aslandukova, A. A., Criniti, G., et al. (2022). Low thermal conductivity of hydrous phase D leads to a self-preservation effect within a subducting slab. *Journal of Geophysical Research: Solid Earth*, *127*, e2022JB024556. https://doi.org/10.1029/2022JB024556

Received 7 APR 2022
Accepted 3 JUN 2022

Author Contributions:

Conceptualization: Wen-Pin Hsieh, Eiji Ohtani
Formal analysis: Wen-Pin Hsieh, Enrico Marzotto
Funding acquisition: Wen-Pin Hsieh
Investigation: Wen-Pin Hsieh, Enrico Marzotto, Leonid Dubrovinsky, Alena A. Aslandukova, Giacomo Criniti, Yi-Chi Tsao, Chun-Hung Lin, Jun Tsuchiya, Eiji Ohtani
Methodology: Wen-Pin Hsieh, Enrico Marzotto, Takayuki Ishii, Leonid Dubrovinsky, Alena A. Aslandukova, Giacomo Criniti, Jun Tsuchiya
Resources: Wen-Pin Hsieh, Takayuki Ishii
Supervision: Wen-Pin Hsieh

Abstract Earth's deep water cycle impacts the physical and chemical properties and geodynamics in its deep interior. However, how dense hydrous magnesium silicates (DHMSs) influence the thermal evolution and dynamics of sinking slabs remains poorly understood. We have precisely measured thermal conductivity of phase D, an important DHMS that could carry large amounts of water from the mantle transition zone to the lower mantle, at high pressure-temperature conditions. The thermal conductivity of (Al,Fe)-bearing phase D is lower than those of the pyrolitic mantle and basaltic crust along slab subduction, except for the depth range of ~800–1,100 km where a spin transition of iron occurs. Numerical simulations indicate that although the spin transition in phase D has minor effects on slab's temperature due to its small volume fraction, the poorly thermally-conductive hydrous minerals contribute to maintain a cold hydrous layer within a sinking slab, stabilizing slab hydrous minerals and promoting water transportation to the deeper mantle.

Plain Language Summary Subduction of the oceanic lithosphere brings water-bearing (hydrous) minerals into the Earth's interior, which could critically influence the thermal evolution and geodynamics of a sinking slab and ambient mantle. Among the hydrous minerals, Phase D is a key phase that could carry large amounts of water from the mantle transition zone (MTZ) to the shallow lower mantle (~1,250 km depth). Here we showed that, compared to the subducting lithosphere and crustal materials, the (Al,Fe)-bearing phase D has a relatively low thermal conductivity at the depths of the MTZ and shallow lower mantle. This might be due to the large amounts of water contained in Phase D (~18 wt.%). The low thermal conductivity of Phase D hinders heat transport through a sinking slab, and thus protects the lithosphere from excessive dehydration. Such effect promotes the survival of hydrous phases to greater depth than previously expected.

1. Introduction

Subduction of oceanic lithosphere can bring water embedded within hydrous minerals into Earth's interior, which would affect physical and chemical properties, rheology, geodynamics, and thermo-chemical evolution of our planet (Hirschmann & Kohlstedt, 2012; Jacobsen, 2006; Nestola & Smyth, 2016; Ohtani, 2020; Ohtani et al., 2018; Peslier et al., 2017). Mineral physics studies showed that dense hydrous magnesium silicates (DHMSs) are a group of minerals which can store large amounts of water (few to ~18 wt.%), much more than the nominally anhydrous minerals (Faccenda, 2014; D. Frost, 1999; Jacobsen, 2006; Ohtani, 2020). Though the DHMSs are only stable at the relatively low temperature of subducting slabs, during slab subduction the DHMSs undergo a series of phase transitions where presence or release of water at different depths could induce local thermal, chemical, and seismic anomalies (Faccenda, 2014; D. Frost, 1999; Ohtani, 2020). Among the DHMSs, phase D with an ideal chemical formula of $MgSi_2H_2O_6$ and ~14–18 wt.% water is of particular importance. Laboratory experiments showed that it is a decomposition product of serpentine at pressures above 22 GPa (L. Liu, 1986, 1987) and remains stable until ~44 GPa (~1,250 km depth) along a slab geotherm, see, for example, (Nishi et al., 2014; Shieh et al., 1998). Such wide range of stability field suggests that the phase D is a key hydrous mineral carrying water from the mantle transition zone (MTZ) to the shallow lower mantle during Earth's deep water circulation.

Writing – original draft: Wen-Pin Hsieh, Enrico Marzotto, Takayuki Ishii, Leonid Dubrovinsky, Alena A. Aslandukova, Jun Tsuchiya, Eiji Ohtani
Writing – review & editing: Wen-Pin Hsieh, Enrico Marzotto, Takayuki Ishii, Leonid Dubrovinsky, Alena A. Aslandukova, Giacomo Criniti, Yi-Chi Tsao, Chun-Hung Lin, Jun Tsuchiya, Eiji Ohtani

In the past decades, many physical and chemical properties of phase D under relevant high pressure (*P*)-temperature (*T*) conditions have been extensively investigated, including its crystal structure, phase relations, equation of state, elastic constants, sound velocities, Raman spectrum, and spin state transition, see, for example, (Y. Chang et al., 2013; D. Frost, 1999; D. J. Frost & Fei, 1999; Daniel J. Frost & Fei, 1998; Ishii et al., 2022; Litasov et al., 2007, 2008; X. Liu et al., 2019; Mainprice et al., 2007; Meier et al., 2021; Nishi et al., 2014; Rosa et al., 2012; Shieh et al., 1998; Tsuchiya et al., 2005; Tsuchiya & Tsuchiya, 2008; Wu et al., 2016; H. Yang et al., 1997). Given the abundance of iron (Fe) and aluminum (Al) in the Earth's mantle, the presence of Fe and Al cations in the phase D could substantially affect its physical properties and, in turn, the transportation and fate of water and iron in Earth's deep interior. Of particular interest is that the Fe-bearing phase D undergoes a pressure-induced spin transition of iron around 37–68 GPa at room temperature (Y. Chang et al., 2013; Wu et al., 2016). Though the contents of ferrous and ferric irons may influence the detailed evolution of phase D's physical properties across the spin transition, sudden drops of unit cell volume and bulk sound velocity are commonly observed. The resulting sound velocity anomaly has been invoked to account for the small-scale seismic heterogeneities observed at the top to middle of the lower mantle (Y. Chang et al., 2013; Wu et al., 2016).

Thermal conductivity of deep Earth materials is essential to influence the temperature profile, thermo-chemical evolution, and geodynamics in Earth's deep interior (Y.-Y. Chang et al., 2017; Dalton et al., 2013; Deschamps & Hsieh, 2019; W.-P. Hsieh et al., 2018; W. P. Hsieh et al., 2017, 2020; Ohta et al., 2012, 2017; Okuda et al., 2019; Y. Xu et al., 2004; Zhang et al., 2019). Recent significant progress on the combination of high-pressure diamond anvil cells with optical pump-probe techniques have enabled precise experimental determinations of the thermal conductivity of Earth materials under relevant extreme *P-T* conditions. Such breakthroughs have shed lights on how heat transfers through the Earth's interior, along with its impacts on the thermal states and geodynamics in different regions (Y.-Y. Chang et al., 2017; Dalton et al., 2013; W.-P. Hsieh et al., 2018; W. P. Hsieh et al., 2017, 2020; Ohta et al., 2012, 2017; Okuda et al., 2019). In particular, previous studies have shown that the hydration-reduced thermal conductivity of mantle minerals, including olivine (Y.-Y. Chang et al., 2017) and ringwoodite (Marzotto et al., 2020), results in a low-temperature condition within a subducting slab, which offers a protection mechanism that allows slab minerals to be transported to the deeper mantle, promoting deep water cycle. However, when a slab sinks through the MTZ and top of the lower mantle, very little is known about the thermal conductivity of DHMSs, in particular, the phase D, and its impact on the surrounding thermo-chemical profile and subduction dynamics. Moreover, the spin state of iron in Fe-bearing minerals, including ferropericlase (W.-P. Hsieh et al., 2018), siderite (Chao & Hsieh, 2019), and δ-(Al,Fe)OOH (W.-P. Hsieh et al., 2020), has been demonstrated to significantly affect their thermal conductivity. The potential effects of spin transition on Fe-bearing phase D's thermal conductivity and on the thermal evolution of sinking slabs have never been investigated.

We here combined ultrafast time-domain thermoreflectance (TDTR) with externally-heated diamond anvil cells (EHDAC) to investigate the effects of Fe and Al on the lattice thermal conductivity of phase D at high *P-T* conditions. The thermal conductivity of (Fe,Al)-bearing phase D is lower than that of the Fe-free, Al-bearing phase D from ambient to ∼78 GPa, except for ∼30–50 GPa where a two-stage spin transition of ferrous and ferric irons occur. Across the spin transition, the thermal conductivity of (Fe,Al)-bearing phase D shows a drastic, 4-fold variation, resulting in an enhanced impurity effect of iron in the low-spin state. Combination of our new data with numerical simulations further demonstrates that the low thermal conductivity of hydrous phases within a subducting slab hinders the heat transfer from ambient mantle to the subducting lithosphere. This causes a low temperature condition that, in turn, enables water to be transported and released to the deeper mantle, potentially influencing local seismic structures as well as the budget and fate of Earth's deep water cycle.

2. Materials and Experimental Methods

2.1. Sample Synthesis and Characterization

Single crystals of Fe-free and Fe-bearing Al-phase D (hereafter Al-phase D and (Al,Fe)-phase D, respectively) were synthesized at 25 GPa and 1,100°C for 4 hr in separate runs with a 1200-ton split-sphere Kawai-type multi-anvil press at Bayerisches Geoinstitut, University of Bayreuth, Germany, see Text S1 in Supporting Information S1 for more details. Chemical compositions and spatial homogeneity of the Al-phase D and (Al,Fe)-phase D were analyzed and confirmed to be $Mg_{1.29}Al_{0.17}Si_{1.73}H_{1.98}O_6$ and $Mg_{1.19}Fe_{0.12}Al_{0.174}Si_{1.71}H_{2.02}O_6$ ($Fe^{3+}/\Sigma Fe = 0.32$), respectively, using an electron microprobe analyzer at Academia Sinica. The samples were

also characterized by X-ray diffraction and synchrotron Mössbauer spectroscopy at ambient and high pressures, indicating a two-stage spin transition of ferrous and ferric irons starting from ~25 GPa (Text S2, S3 and Figures S1–S3 in Supporting Information S1).

2.2. Sample Preparation for High Pressure Experiments

Each of the phase D samples was polished down to ~10 μm thick and then coated with ~80 nm thick Al thin film that serves as the thermal transducer for thermal conductivity measurement. The phase D sample, along with several ruby spheres, was then loaded into a symmetric piston-cylinder diamond anvil cell (DAC) where a pair of 300 μm culet anvils and a Re gasket were used. For high pressure and room temperature measurements, silicone oil (ACROS ORGANICS with CAS No. 63148-62-9) was used as the pressure medium. For simultaneous high *P-T* measurements, we used polycrystalline NaCl powder as the pressure medium that was first thermally dried at ~120°C for about one hour. We characterized the pressure within the sample chamber by monitoring the shifts of fluorescence and Raman spectrum of ruby spheres (Dewaele et al., 2004), as well as the Raman spectrum of diamond anvil when it is applicable (Akahama & Kawamura, 2004). The pressure uncertainty is typically <5% over the pressure range we studied. At pressures higher than ~60 GPa at room temperature, we estimated the pressure uncertainty to be <5 GPa, by comparing the pressures inferred from the Raman spectra of the diamond anvil and ruby spheres (see, e.g., W.-P. Hsieh, 2021).

To create simultaneous high *P-T* conditions, for example, 40.5 GPa and 723 K in the present study, we used an externally heated BX-90 DAC (EHDAC) that offers a spatially homogeneous high *T* environment within the sample chamber. Details of the EHDAC and pressure uncertainty during high *P-T* measurements can be found in (W.-P. Hsieh, 2021; Lai et al., 2020).

2.3. Lattice Thermal Conductivity Measurements

We used TDTR combined with the DAC to study the thermal conductivity of phase D at high pressure and room temperature conditions. For simultaneous high *P-T* thermal conductivity measurements, we used the TDTR along with the EHDAC. TDTR has been a well-established ultrafast optical pump-probe method that enables precise measurement of thermal conductivity at ambient and high pressures, see, for example, (Y.-Y. Chang et al., 2017; W.-P. Hsieh et al., 2018; W. P. Hsieh et al., 2020). The detailed operation principles of the TDTR were described in literature, see, for example (Cahill, 2004; W. P. Hsieh et al., 2009; Kang et al., 2008). In short, we split the output of a Ti:sapphire oscillator laser into pump and probe pulses. The pump pulse was electro-optically modulated at 8.7 MHz and went through a mechanical delayed stage which dynamically changed the time the pump pulse hit the sample. The pump pulse finally heated up the Al film transducer coated on the sample, creating a temperature variation. The probe pulse, on the other hand, measured the resulting changes in the optical reflectivity of Al caused by the pump pulse heating. We used a fast silicon photodiode combined with a high-frequency lock-in amplifier to detect the subtle changes in the reflected probe pulse intensity, which includes a complex signal of the in-phase V_{in} (real part) and out-of-phase V_{out} (imaginary part).

We determined the lattice thermal conductivity of phase D by comparing the TDTR spectrum, that is, the ratio $-V_{in}/V_{out}$ as a function of delay time, with calculations based on a bi-directional thermal diffusion model. In the thermal model, we simulated the dynamics of heat transfer from the Al film to the phase D sample and the pressure medium (Schmidt et al., 2008). A set of example data along with thermal model calculations was shown in Figure S4 of Supporting Information S1. As listed in the Table S1 of Supporting Information S1, our thermal model contains a number of parameters that control the heat transfer dynamics within the DAC, including thermal conductivity, volumetric heat capacity, and thickness of each layer (i.e., phase D sample, Al film transducer, and pressure medium) within the sample chamber. The phase D's thermal conductivity, however, is the only significant unknown that is determined by fitting the model calculation to the experimental data. The high-pressure, room-temperature thermal conductivity and volumetric heat capacity of the Al film and silicone oil were from previous data (W.-P. Hsieh, 2015; W. P. Hsieh et al., 2009). At high *P-T* conditions, the heat capacity of Al was estimated based on its atomic density, elastic constants, and Debye temperature, see (W. P. Hsieh et al., 2009), while the thermal conductivity and heat capacity of the pressure medium NaCl were from (W.-P. Hsieh, 2021). The volumetric heat capacity of phase D is described in Section 2.3.

We used picosecond acoustics (O'Hara et al., 2001) to *in situ* measure the Al thickness at ambient conditions. However, the acoustic echo was substantially reduced when the sample was compressed to high pressures. To estimate how the Al thickness changes under high *P-T* conditions, we took a method developed by Chen et al. (2011) and considered the effect of thermal expansion of Al upon heating (W.-P. Hsieh, 2021). The thickness of phase D, silicone oil, and NaCl are all initially ∼10–15 μm, much longer than their thermal penetration depths (i.e., a depth that the pumped thermal wave can diffuse into a material) of ∼1 μm (W.-P. Hsieh, 2021; W. P. Hsieh et al., 2009). Thus, changes and uncertainties in their thicknesses under high *P-T* conditions have very minor effects on the thermal model calculations. We note that the estimated uncertainty of the thermal conductivity of phase D is primarily from the data analysis, that is, the uncertainties of the input parameters used in the thermal model. The uncertainties in all the input parameters would propagate ∼10%–15% error in the thermal conductivity of phase D below 30 GPa, and ∼15%–20% error at 30–75 GPa. As we show in the Supporting Information S1, an uncertainty of an input parameter leads to a systematic shift of all the thermal conductivity of phase D at a given *P-T* condition, see Figure S5 in Supporting Information S1 for the details of the TDTR sensitivity analysis and (Zheng et al., 2007) for uncertainty evaluations.

2.4. Calculations of the Heat Capacity of Phase D at High Pressures

We conducted first principles calculation based on density functional theory to estimate the heat capacity and equation of state of phase D with an ideal chemical formula $MgSi_2O_6H_2$. Details of the computational method can be found in (W. Hsieh et al., 2020). In our calculations, the exchange correlation functional (Perdew et al., 1996) was described by generalized gradient approximation (GGA-PBE). We imposed a kinetic cut-off of 80 Ry for planewave expansion of the projector augmented-wave (PAW) potentials (Blöchl, 1994). The structures of asymmetric and symmetric hydrogen bond were fully relaxed at −1, 0, 5, 10, 15, 20, 25, 30 and 40, 50, 60, 70, 80, 90, 100, 120, and 150 GPa, respectively, until the residual forces were $<1.0 \times 10^{-5}$ Ry/au. The irreducible Brillouin zone of phase D was sampled on $5 \times 5 \times 4$ Monkhorst-Pack mesh (Monkhorst & Pack, 1976). We employed the structure model of $MgSi_2O_6H_2$ phase D with the ordered hydrogen positions used in previous study (Tsuchiya et al., 2005; Tsuchiya & Tsuchiya, 2008). After the structure fully relaxed, the phonon vibrational frequencies were computed by density functional perturbation theory (Baroni et al., 2001). The Helmholtz free energy within quasi harmonic approximation (QHA) was obtained by sampling the dynamical matrices on a $3 \times 3 \times 4$ $\boldsymbol{q}$-grid (19 q-points), and then interpolating the force constant matrices on denser meshes. As such, the heat capacity at constant pressure C_P can be derived from standard thermodynamic relations. Thermodynamic properties of $MgSi_2O_6H_2$ phase D show anomalous behaviors around 40 GPa and we found that QHA is invalid. These behaviors are correlated with the symmetrization of hydrogen bonds in phase D (Tsuchiya et al., 2005). Those are very similar to our previous study of δ-AlOOH (W.-P. Hsieh et al., 2020). Except for ∼40 GPa, C_P of phase D is nearly a constant of ∼2.9 J cm^{-3} K^{-1} at room temperature and 0–100 GPa. Pressure dependence of the volumetric heat capacity C_p of $MgSi_2O_6H_2$ phase D is shown in Table S2 of Supporting Information S1. Due to the computational complexity, we did not calculate the volumetric heat capacity of Al-phase D and (Al,Fe)-phase D as a function of pressure. Previous studies suggested that when incorporated with ∼10–15 at% impurities, the heat capacity of (Mg,Fe)O and δ-(Al,Fe)OOH remain similar to that of the MgO (Fukui et al., 2012) and δ-AlOOH (W.-P. Hsieh et al., 2020), respectively. We thus assumed that the volumetric C_P of our Al-phase D and (Al,Fe)-phase D is similar to the $MgSi_2O_6H_2$ phase D. The uncertainty due to the heat capacity of phase D is considered in our data analysis and uncertainty estimation (Figure S5 in Supporting Information S1).

3. Experimental Results

3.1. High-Pressure, Room-Temperature Thermal Conductivity Across Spin Transition of Iron

The thermal conductivity of randomly-oriented single crystals of Al-phase D ($\Lambda_{\text{Al-phase D}}$) and (Al,Fe)-phase D ($\Lambda_{\text{AlFe-phase D}}$) at high pressure and room temperature are presented in Figure 1. Several measurement runs were performed for each composition that show consistent results. The $\Lambda_{\text{Al-phase D}}$ (black symbols in Figure 1) is 3.5 W m^{-1} K^{-1} at ambient conditions, and monotonically increases with pressure to ∼26 W m^{-1} K^{-1} at 74 GPa. However, when incorporated with iron (red symbols in Figure 1), the pressure evolution of thermal conductivity significantly changes. At ambient conditions, the $\Lambda_{\text{AlFe-phase D}}$ is slightly reduced to 2.5 W m^{-1} K^{-1}, presumably due to the additional phonon scattering by iron impurity that reduces the phonon group velocity and mean-free-path. Upon initial compression, the $\Lambda_{\text{AlFe-phase D}}$ slowly increases with pressure until ∼26–30 GPa where the

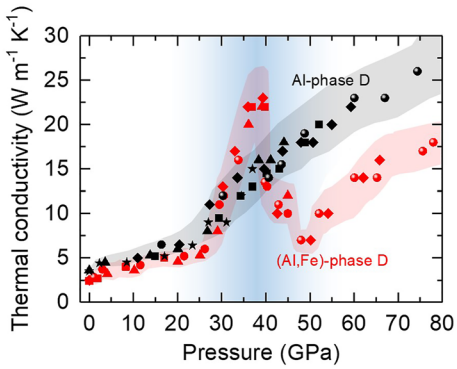

Figure 1. High-pressure, room temperature lattice thermal conductivity of Al-phase D (black symbols) and (Al,Fe)-phase D (red symbols). We performed several runs of measurement for each composition that yield consistent results. Different symbol shape represents different crystal orientation. The shaded area next to each data set indicates its estimated uncertainty that is primarily from the uncertainties of the thermal model parameters used in data analysis, see, for example, Figure S5 in Supporting Information S1. Both sets of the thermal conductivity data would systematically shift if an uncertainty of a parameter is applied. The blue vertically shaded area illustrates the pressure range of the spin transition of iron in (Al,Fe)-phase D.

spin transition of ferrous iron occurs (Text S3 in Supporting Information S1). Through the spin transition of ferrous and then ferric irons, the $\Lambda_{\text{AlFe-phase D}}$ drastically peaks to 23 W m^{-1} K^{-1} at ~40 GPa, followed by a drop down to 7 W m^{-1} K^{-1} at 50 GPa. Further increasing pressure raises the $\Lambda_{\text{AlFe-phase D}}$ to 18 W m^{-1} K^{-1} at 78 GPa, ~30% lower than the $\Lambda_{\text{Al-phase D}}$ at such pressure. Note that for both Al-phase D and (Al,Fe)-phase D, the thermal conductivity in each measurement run (different crystal orientation) is similar to each other, suggesting that the effect of crystal orientation on their thermal conductivity is negligible. Furthermore, similar to the ferropericlase (W.-P. Hsieh et al., 2018) and δ-(Al,Fe)OOH (W.-P. Hsieh et al., 2020), we observed an enhanced impurity effect of iron in the low-spin Fe-bearing phase D, that is, compared to the high-spin state, the thermal conductivity of low-spin Fe-bearing phase D is much lower than that of the Fe-free phase D.

We note that the anomalous pressure evolution of $\Lambda_{\text{AlFe-phase D}}$, that is, few-fold, drastic variation, across the spin transition of iron is similar to that observed in δ-(Al,Fe)OOH (W.-P. Hsieh et al., 2020) and $(Fe_{0.78}Mg_{0.22})CO_3$ siderite (Chao & Hsieh, 2019). The physical mechanism that influences the thermal conductivity evolution of Fe-bearing phase D, however, is expected to be more complex than in δ-(Al,Fe)OOH and $(Fe_{0.78}Mg_{0.22})CO_3$, since it involves a two-stage spin state transition of ferrous and ferric irons. Detailed theoretical and computational investigations are required to decipher the complex physics and anomalous thermal conductivity evolution through the two-stage spin transition in Fe-bearing phase D.

3.2. High Pressure-Temperature Thermal Conductivity Measurements

We further performed two sets of simultaneous high *P-T* measurements on the (Al,Fe)-phase D (Figure 2). Though our measurement temperature was only raised to ~723 K, a temperature dependence was clearly presented. In both sets of measurements (P = 26 and 40.5 GPa), the $\Lambda_{\text{AlFe-phase D}}$ decreases as the temperature increases. We note that changes in the pressure caused by the heating were *in situ* characterized to be <6 GPa, depending on the initial pressure and heating temperature; such effect has been calibrated in our data analysis (W.-P. Hsieh, 2021). To obtain the temperature dependence of $\Lambda_{\text{AlFe-phase D}}$ at high pressures, we assume the $\Lambda_{\text{AlFe-phase D}}$ follows a temperature dependence $\Lambda(T) = a\Lambda_{RT}T^n$, where a is a normalization constant and Λ_{RT} the thermal conductivity at room temperature. By converting Figure 2 data into a lnΛ-ln$T$ plot, we determine the value n (linear slope in lnΛ-ln$T$ plot) to be −0.46(±0.12) and −0.55(±0.2) for $\Lambda_{\text{AlFe-phase D}}$ at 26 and 40.5 GPa, respectively. Both n values are in reasonable agreement with the typically reported value of approximately −0.5 for an Fe-bearing mineral (Dalton et al., 2013; W.-P. Hsieh et al., 2018; Y. Xu et al., 2004; Zhang et al., 2019).

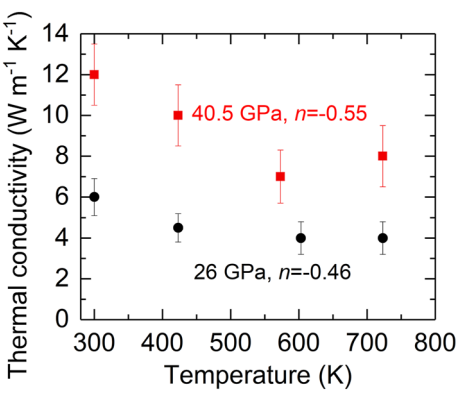

Figure 2. Temperature dependence of thermal conductivity of (Al,Fe)-bearing phase D at 26 (black circles) and 40.5 GPa (red squares). Both sets of data show that the thermal conductivity follows a power law of $\Lambda(T)$ scaling with T^n, where n = −0.46 and −0.55 for the thermal conductivity at 26 and 40.5 GPa, respectively.

4. Discussions and Geophysical Implications

4.1. Modeling of the Thermal Conductivity of Phase D Along a Slab Geotherm

To understand how the low thermal conductivity of hydrous phase D impacts the thermal evolution of a subducting slab, we first model the thermal conductivity of phase D along a representative geotherm of a sinking slab which is assumed to be 800 K colder than that of a regular mantle (Katsura et al., 2010). For (Al,Fe)-phase D, we assumed the temperature dependence of $\Lambda_{\text{AlFe-phase D}}$ follows that obtained in Figure 2, that is, Λ scales with $T^{-1/2}$. Given the fact that both Al and Fe ions are impurities in the phase D crystal, the temperature dependence of $\Lambda_{\text{Al-phase D}}$ is expected to also follow the $T^{-1/2}$ dependence. In Figure 3, we plot the modeled thermal conductivity of Al-phase D and (Al,Fe)-phase D as a function of depth, along with that of

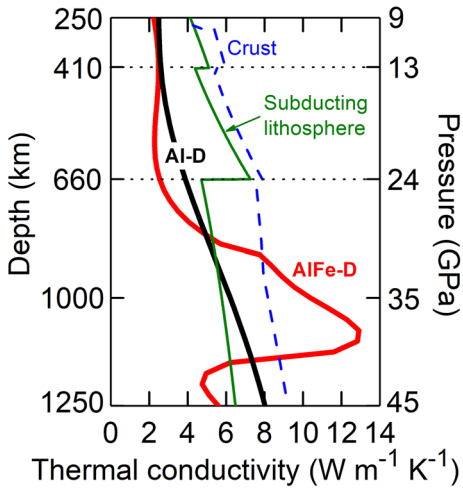

Figure 3. Modeled thermal conductivity of Al-phase D (Al-D, black curve) and (Al,Fe)-phase D (AlFe-D, red curve) along a representative slab geotherm. Both Al-phase D and (Al,Fe)-phase D have much lower thermal conductivity than the subducting lithosphere (green curve) and crust (blue dashed curve) above ~800 km depth. The thermal conductivity of subducting lithosphere is assumed to be that of dry olivine at 250–410 km (Y.-Y. Chang et al., 2017), dry ringwoodite at 410–660 km (Marzotto et al., 2020), and an aggregate with 80 vol% (Fe,Al)-bearing bridgmanite and 20 vol% ferropericlase at 660–1,250 km (W.-P. Hsieh et al., 2018), see Text S4 in Supporting Information S1 for details. The thermal conductivity of subducting oceanic crust is assumed to be that of an aggregate with 10 vol% pure stishovite that appears after 300 km depth (Text S4 in Supporting Information S1 and (W.-P. Hsieh et al., 2022)) and 90 vol% dry olivine and ringwoodite in the upper mantle and transition zone, respectively; in the lower mantle it is composed of 60 vol% (Fe,Al)-bearing bridgmanite, 20 vol% Fe-bearing new-hexagonal-aluminous phase, and 20 vol% stishovite (Text S4 in Supporting Information S1 and (W.-P. Hsieh et al., 2022)).

the subducting lithosphere and oceanic crust. During slab subduction, both the $\Lambda_{\text{Al-phase D}}$ (Al-D, black curve) and $\Lambda_{\text{AlFe-phase D}}$ (AlFe-D, red curve) are much lower than the subducting lithosphere (green curve) and oceanic crust (blue dashed curve), including at the depths of the MTZ and top of the lower mantle, where the phase D is expected to be present (Litasov et al., 2008; C. Xu & Inoue, 2019). At deeper depth of ~800–1,100 km, the spin transition of iron in (Al,Fe)-phase D raises its thermal conductivity to a maximum of 12.9 W m^{-1} K^{-1}, ~50% larger than that of the crust, at ~1,050 km depth. Such transition switches the role of (Al,Fe)-phase D from a thermal insulator at shallower depth to a thermal conductor as the slab sinks to deeper mantle.

4.2. Numerical Modeling of the Hydration Effects on the Thermal Evolution of a Sinking Slab

We further conducted numerical simulations to understand how the poorly thermally-conductive hydrous minerals impact the thermal evolution of a sinking slab. The simulation was based on a self-written Matlab code with re-arrangements from the one performed by Marzotto et al. (2020) and W.-P. Hsieh et al. (2022). Details of our numerical modeling are described in Text S4–S7 of Supporting Information S1. In short, we designed a 1D numerical model in which a cold slab was vertically subducted, and heated by the warm ambient mantle (Figure 4). For simplicity, the 1D slab was made of three lithologies (Figure S6 in Supporting Information S1), including (*a*) an 8 km-thick oceanic crust with mid-ocean ridge basalt (MORB) composition (Marquardt & Thomson, 2020), (*b*) a 3 km-thick hydrated harzburgitic lithosphere (John et al., 2011), and (*c*) a 106 km-thick dry harzburgitic lithosphere (Irifune & Ringwood, 1987). The domain boundaries were made of 0.1 km-thick pyrolitic mantle (Marquardt & Thomson, 2020). The initial temperature profile of an 80 Myrs-old slab (Stein & Stein, 1992) was first calculated by solving the analytical solution for the half-space cooling (Stage 1 in Figure 4) (D. L. Turcotte & Schubert, 2014). We assigned a constant sinking velocity v_{sink}(cm yr^{-1}) for the slab that sinks through three different regions of the mantle: upper mantle (Stage 2 in Figure 4), MTZ (Stage 3), and lower mantle (Stage 4). The mineral assemblage in each layer of the slab was updated with the lithology stable in the given mantle region (Text S4 in Supporting Information S1). We ignored the latent heat during the phase transition, and we neglected adiabatic compression by assuming a constant mantle temperature T_{mantle} = 1600 K. The governing equations of the depth (i.e., *P-T*) dependent thermal conductivity Λ, density ρ, and heat capacity *Cp* for each lithology were parameterized from the mineral physics datasets reported from the present study and literature (Text S4–S5, Figure S7, Tables S3–S5 in Supporting Information S1). To simplify the calculations, we opted to use the average slab temperature T^t_{ave} at the instant *t* to calculate the *T*-dependent thermal properties of the slab (Text S4–S5 in Supporting Information S1).

Our modeling focuses on how the hydration influences the thermal state of a sinking slab during subduction. As illustrated in Figure 4, the thin hydrous layer (light blue) through serpentinization appears in the slab upon subduction, and is maintained from the upper mantle down to mid-lower mantle. Because coesite transforms to stishovite at ~300 km depth (Aoki & Takahashi, 2004), for simplicity, the lithospheric slab and meta-basaltic crust are modeled to have the same physical properties, for example, $\Lambda_{LitSlab} = \Lambda_{MORB}$ before the slab crosses 300 km depth. We run six different scenarios (Figure 5): (a) the lithospheric slab is made of dry olivine and no serpentinization (solid green curve); (b) the lithospheric slab is made of dry olivine and the hydrous layer has intermediate serpentinization (volume fraction of DHMS, e.g., phase D, X_D = 0.15, solid red curve); (c) the lithospheric slab is made of dry olivine and the hydrous layer has high serpentinization (X_D = 0.3, solid blue curve); (d) the lithospheric slab is made of wet olivine and no serpentinization (dashed green curve); (e) the lithospheric slab is made of wet olivine and the hydrous layer has intermediate serpentinization (X_D = 0.15, dashed red curve); (f) the lithospheric slab is made of wet olivine and the hydrous layer has high serpentinization (X_D = 0.3, dashed blue curve), see Text S4–S5 in Supporting Information S1 for details of each layer's thermal conductivity

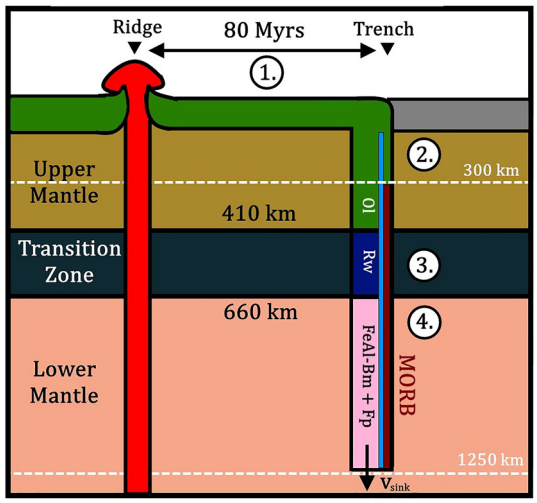

Figure 4. Sketch of the four stages of the model: (1) an 80 Myrs-old slab undergoes half-space cooling (Turcotte & Schubert, 2014); at the trench, the slab sinks down through (2) the upper mantle (<410 km), (3) the transition zone (410–660 km), and (4) the lower mantle (660–1,250 km). We assumed the slab lithosphere is made of olivine (<410 km in green), ringwoodite (410–660 km in blue), and (Fe,Al)-bridgmanite and ferropericlase (>660 km in pink). After 300 km depth, SiO_2 stishovite is present in the subducted basaltic crust (mid-ocean ridge basalt (MORB) in maroon). The thin hydrous layer with dense hydrous magnesium silicates sandwiched between the subducting lithosphere and crust is indicated in light blue.

under different scenarios. We repeated the six modeled scenarios with three different slab sinking velocities v_{sink} (Syracuse et al., 2010): fast (5 cm yr^{-1}), medium (3 cm yr^{-1}), and slow (1 cm yr^{-1}) subduction. To quantitatively understand the thermal evolution of each modeled scenario, we calculated the temperature profile at the base of the hydrous layer (T_{base}, Figures 5a–5c), and the average temperature of the slab (T_{ave}, Figures 5d–5f).

4.3. Effects of Hydration-Induced Low Temperature on Phase Transition Depths of Slab Minerals and Fate of Sinking Slabs

Figure 5 and Table 1 show that, compared to the slow subduction, the mediate and fast subduction hinder thermal equilibration of the slab with the ambient mantle, that is, causing larger temperature gradient through the oceanic crust and hydrous layer. Moreover, though the hydrous layer is only few-km-thick and phase D represents a small volume fraction of a sinking slab, when present (scenario II and III), its low thermal conductivity results in a T_{base} that is ~10–20 K colder than that without serpentinization (scenario I) at 410 and 660 km depths (Table 1). The ~4-fold drastic increase of (Al,Fe)-phase D's thermal conductivity across the spin transition, however, has a minor effect on the T_{base} (only few K increase), due to its small volume fraction and the limited pressure range in which the peak $\Lambda_{AlFe\text{-}phase\ D}$ is reached. On the other hand, with the same extent of serpentinization, the T_{base} of a hydrated subducting lithosphere (scenario IV-VI) is ~50–100 K colder than the dry one (scenario I-III). It is evident that the presence of hydrous phases (NAMs and DHMSs) significantly hinders the heat transfer into a sinking slab, resulting in a colder environment that can preserve hydrous minerals during

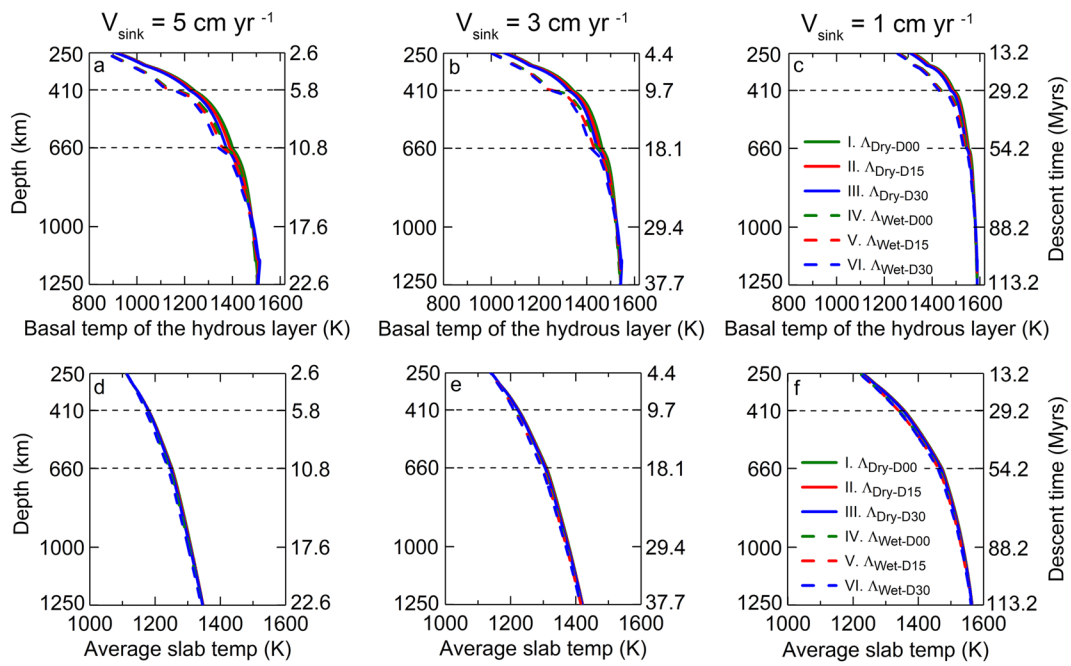

Figure 5. Thermal evolution of a sinking slab with different serpentinization (content of phase D). (a–c) Depth-descent time dependence of the temperature at the base of the hydrous layer T_{base}. (d–f) Average slab temperature T_{ave}. Different curve in each subplot represents the temperature evolution when the slab sinks into the mantle (250–1,250 km) for the given scenario I–VI (see text for the details). Three different sinking velocity v_{sink} (fast, medium, and slow as labeled on the top) were tested for each given scenario. The low thermal conductivity due to the hydration, including the phase D in the peridotite layer and hydrous olivine and ringwoodite in lithospheric slab, delays the thermal equilibration with the ambient mantle and enhances the low temperature anomaly (lower T_{base} and T_{ave}) within a sinking slab.

Table 1
Comparison of the Temperatures at the Base of the Crust $T_{base}(K)$ for a Given Depth, for Example, d = 410/660/1,250 km

	T^{I}_{base}	T^{II}_{base}	T^{III}_{base}	T^{IV}_{base}	T^{V}_{base}	T^{VI}_{base}
v_{sink} = 5 cm yr^{-1}						
410 km	1,239	1,231	1,219	1,147	1,140	1,132
660 km	1,401	1,390	1,375	1,373	1,359	1,343
1,250 km	1,509	1,509	1,508	1,506	1,506	1,505
v_{sink} = 3 cm yr^{-1}						
410 km	1,343	1,334	1,323	1,247	1,240	1,234
660 km	1,464	1,455	1,443	1,440	1,429	1,415
1,250 km	1,543	1,543	1,543	1,541	1,541	1,541
v_{sink} = 1 cm yr^{-1}						
410 km	1,490	1,485	1,477	1,430	1,426	1,421
660 km	1,553	1,549	1,544	1,543	1,538	1,532
1,250 km	1,590	1,589	1,589	1,589	1,589	1,589

Note. Each column indicates a different scenario I–VI.

subduction (Y.-Y. Chang et al., 2017). The delay in the heating of the slab is proportional to the amount of water contained in the hydrous layer, and to its thickness (Marzotto et al., 2020). Interestingly, the pressure evolution of thermal conductivity of the (Al,Fe)-phase D is similar to that of the hydrous δ-(Al,Fe)OOH, where the spin transition of iron also triggers a drastic variation of thermal conductivity (W.-P. Hsieh et al., 2020). Moreover, at the depths of the MTZ and top of the lower mantle, the thermal conductivity of the δ-(Al,Fe)OOH is as low as that of (Al,Fe)-phase D. If the δ-(Al,Fe)OOH also appears in the basaltic crust at these depths (Ishii et al., 2022; X. Liu et al., 2019), it would further enhance the cold environment within a subducting slab.

The stability field of slab minerals could be altered when the minerals experience a local temperature anomaly during subduction. For instance, serpentine breaks down and transforms to a series of DHMSs, including an assemblage of phase A and enstatite at ~200 km depth (~6 GPa), phase E and enstatite and wadsleyite at ~380 km (~13 GPa), superhydrous phase B and stishovite and ringwoodite at ~470 km (~16 GPa), and phase D and bridgmanite and ferropericlase at ~600 km (~22 GPa), along a cold slab geotherm, see, for example, (D. Frost, 1999; Ohtani, 2020). These DHMSs typically decompose as the local temperature is higher than ~1,400–1,500 K (Ohtani, 2020). However, our simulations suggest that in fast sinking slabs with high serpentinization, such as Tonga subduction zone (Goes et al., 2017; Wei et al., 2017), metastable DHMSs could be present at greater depth than expected, due to the hydration-induced low temperature conditions. Compared to the dry slab (scenario I), a colder T_{base} by ~50–100 K resulted from the hydration-reduced thermal conductivity of hydrous slab minerals (e.g., scenario V and VI) at the upper mantle and transition zone depths could delay the breakdown of DHMS, allowing them to transport water to the deeper mantle. Importantly, the breakdown of phase D and the consequent release of water to the neighboring crust and mantle would promote the hydration melting of subducted MORB and mantle minerals, such as bridgmanite, in the region (Schmandt et al., 2014). This in turn would not only result in a regional seismic low velocity zone at greater depth than expected (C. Xu & Inoue, 2019), but also form a locally stishovite-enriched region (Amulele et al., 2021), altering regional seismic and mineralogical features.

In addition to the DHMSs, hydration could also influence the phase transition depth of mantle minerals. Mineral physics experiments showed that olivine transforms to wadsleyite at ~410 km depth with a positive Clapeyron slope of ~2.5–4 MPa K^{-1} (Katsura et al., 2004; Katsura & Ito, 1989), and then to ringwoodite at ~520 km depth with a positive Clapeyron slope of ~5–6.9 MPa K^{-1} (Katsura & Ito, 1989; Suzuki et al., 2000). The temperature at the top of a hydrous subducting lithosphere (scenario V and VI) is ~50–100 K colder than that of scenario I. Such low temperature anomaly is expected to upshifts the olivine-wadsleyite transition depth by ~4–12 km and the wadsleyite-ringwoodite transition depth by ~7–20 km, affecting the topography of the mantle discontinuities (Helffrich, 2000).

Furthermore, prior studies have shown that transformation kinetics of metastable minerals in a subducting slab could be affected by the hydration effect as well. Hydration helps delay transformations of metastable olivine (Kubo et al., 1998) and pyroxene (van Mierlo et al., 2013) into deeper regions in slab's core conditions, which can promote slab stagnation around the 660 km depths (Fukao & Obayashi, 2013) and deep-focus earthquakes (e.g., (Zhan, 2020)). (Ishii & Ohtani, 2021) demonstrated that olivine that coexists with hydrous phase A is dry, suggesting a strong water partitioning into hydrous minerals, remaining nominally anhydrous minerals dry. This results in the formation of metastable olivine in a cold slab's core even in a wet subducting slab. If this is the case, the hydration effect further protects metastable minerals in the cold slab's core.

We finally note that the hydration-induced low thermal conductivity is expected to be general for other DHMSs. Thermal conductivity of a material is positively correlated with its elastic moduli (Ashcroft & Mermin, 1976; W.-P. Hsieh et al., 2018). Given the fact that the elastic moduli of other DHMSs, including phase A (Sanchez-Valle et al., 2008), phase E (Satta et al., 2019; Shieh et al., 2000), and superhydrous phase B (D. Yang et al., 2017), are smaller or comparable to those of phase D (Y. Chang et al., 2013; Litasov et al., 2008), their thermal conductivities

would follow such trend. This will strengthen our findings that the presence of poorly thermally-conductive DHMSs would help maintain a low temperature condition within a subducting slab, forming a self-protection mechanism for slab minerals to be transported to the deeper mantle.

5. Conclusions

Using the combination of EHDAC and ultrafast TDTR, we have precisely measured the thermal conductivity of Al-phase D and (Al,Fe)-phase D under high pressure and elevated temperatures. Similar to several Fe-bearing minerals, the thermal conductivity of (Al,Fe)-phase D changes drastically through the spin transition of iron, leading to an enhanced impurity effect of iron in its low-spin state. Our data modeling shows that for a sinking slab, the poorly thermally-conductive phase D contributes to the formation of a thin thermal insulating layer sandwiched between the oceanic crust and subducting lithosphere. Numerical simulations further indicate that the low thermal conductivity of hydrous minerals results in a lower temperature profile within a slab. This enables slab minerals to carry water to deeper mantle than expected, which may influence local seismic and mineralogical characteristics. Further detailed investigations on the thermal conductivity of other DHMSs, such as phase A, phase E, superhydrous phase B, and phase H, along relevant geotherm pressure-temperature conditions will provide more comprehensive thermal conductivity evolution of DHMSs during slab subduction, where thermal conductivity discontinuities may be present across the phase transitions between DHMSs. Combined with numerical geodynamics modeling, this would significantly advance our understanding of the thermal states of sinking slab and surrounding mantle, with insights into the route of water transportation and its effects on the complex thermal, chemical, seismic, and geodynamical anomalies.

Data Availability Statement

Our data are stored in the Zenodo repository with a https://doi.org/10.5281/zenodo.6378130. https://zenodo.org/record/6378131#.YjqTrXpBw2w.

Acknowledgments
This work was partially supported by the Academia Sinica and the Ministry of Science and Technology (MOST) of Taiwan, Republic of China, under Contract AS-IA-111-M02 and MOST 110-2628-M-001-001-MY3. This work was also supported by the Grants-in-Aid of the German Research Foundation (no. IS350/1-1 for TI). WPH acknowledges the fellowship from the Foundation for the Advancement of Outstanding Scholarship, Taiwan. EM has been supported by DFG (Grant No. GRK 2156/1) and the JSPS Japanese-German graduate externship. We also thank Dr. Yoshiyuki Iizuka and Mr. Chao-Chih Chen of Academia Sinica for their help with the EPMA and TDTR experiments.

References

Akahama, Y., & Kawamura, H. (2004). High-pressure Raman spectroscopy of diamond anvils to 250 GPa: Method for pressure determination in the multimegabar pressure range. *Journal of Applied Physics*, *96*, 3748–3751. https://doi.org/10.1063/1.1778482

Amulele, G., Karato, S. I., & Girard, J. (2021). Melting of bridgmanite under hydrous shallow lower mantle conditions. *Journal of Geophysical Research: Solid Earth*, *126*, e2021JB022222. https://doi.org/10.1029/2021JB022222

Aoki, I., & Takahashi, E. (2004). Density of MORB eclogite in the upper mantle. *Physics of the Earth and Planetary Interiors*, *143*(1–2), 129–143. https://doi.org/10.1016/j.pepi.2003.10.007

Ashcroft, N. W., & Mermin, N. D. (1976). Solid state physics (p. 500).

Baroni, S., de Gironcoli, S., Dal Corso, A., & Giannozzi, P. (2001). Phonons and related crystal properties from density-functional perturbation theory. *Reviews of Modern Physics*, *73*, 515–562. https://doi.org/10.1063/1.3563634

Blöchl, P. (1994). Projecto augmented-wave method. *Physical Review B: Condensed Matter*, *50*(24), 17953. https://doi.org/10.1142/9789814365031_0023

Cahill, D. G. (2004). Analysis of heat flow in layered structures for time-domain thermoreflectance. *Review of Scientific Instruments*, *75*(12), 5119–5122. https://doi.org/10.1063/1.1819431

Chang, Y., Jacobsen, S. D., Lin, J., Bina, C. R., Thomas, S., Wu, J., et al. (2013). Spin transition of Fe3+ in Al-bearing phase D: An alternative explanation for small-scale seismic scatterers in the mid-lower mantle. *Earth and Planetary Science Letters*, *382*, 1–9. https://doi.org/10.1016/j.epsl.2013.08.038

Chang, Y.-Y., Hsieh, W.-P., Tan, E., & Chen, J. (2017). Hydration-reduced lattice thermal conductivity of olivine in Earth' s upper mantle. *Proceedings of the National Academy of Sciences*, *114*(16), 4078. https://doi.org/10.1073/pnas.1616216114

Chao, K.-H., & Hsieh, W.-P. (2019). Thermal conductivity anomaly in (Fe0.78Mg0.22)CO3 siderite across spin transition of iron. *Journal of Geophysical Research: Solid Earth*, *124*, 1388–1396. https://doi.org/10.1029/2018jb017003

Chen, B., Hsieh, W.-P., Cahill, D. G., Trinkle, D. R., & Li, J. (2011). Thermal conductivity of compressed H2O to 22 GPa: A test of the Leibfried-Schlömann equation. *Physical Review B*, *83*(13), 132301. https://doi.org/10.1103/PhysRevB.83.132301

Dalton, D. A., Hsieh, W.-P., Hohensee, G. T., Cahill, D. G., & Goncharov, A. F. (2013). Effect of mass disorder on the lattice thermal conductivity of MgO periclase under pressure. *Scientific Reports*, *3*, 2400. https://doi.org/10.1038/srep02400

Deschamps, F., & Hsieh, W.-P. (2019). Lowermost mantle thermal conductivity constrained from experimental data and tomographic models. *Geophysical Journal International*, *219*, S115–S136. https://doi.org/10.1093/gji/ggz231

Dewaele, A., Loubeyre, P., & Mezouar, M. (2004). Equations of state of six metals above 94 GPa. *Physical Review B*, *70*(9), 094112. https://doi.org/10.1103/PhysRevB.70.094112

Faccenda, M. (2014). Water in the slab: A trilogy. *Tectonophysics*, *614*, 1–30. https://doi.org/10.1016/j.tecto.2013.12.020

Frost, D. (1999). The stability of dense hydrous magnesium silicates in Earth' s transition zone and lower mantle. *Mantle Petrology*(6), 283.

Frost, D. J., & Fei, Y. (1998). Stability of phase D at high pressure and high temperature. *Journal of Geophysical Research*, *103*(4), 7463–7474. https://doi.org/10.1029/98jb00077

Frost, D. J., & Fei, Y. (1999). Static compression of the hydrous magnesium silicate phase D to 30 GPa at room temperature. *Physics and Chemistry of Minerals*, *26*(5), 415–418. https://doi.org/10.1007/s002690050202

Fukao, Y., & Obayashi, M. (2013). Subducted slabs stagnant above, penetrating through, and trapped below the 660 km discontinuity. *Journal of Geophysical Research: Solid Earth*, *118*(June), 5920–5938. https://doi.org/10.1002/2013JB010466

Fukui, H., Tsuchiya, T., & Baron, A. Q. R. (2012). Lattice dynamics calculations for ferropericlase with internally consistent LDA+U method. *Journal of Geophysical Research*, *117*, B12202. https://doi.org/10.1029/2012JB009591

Goes, S., Agrusta, R., Hunen, J. V., & Garel, F. (2017). Subduction-transition zone interaction: A review. *Geosphere*, *13*(3), 1–21. https://doi.org/10.1130/GES01476.1

Helffrich, G. (2000). Topography discontinuities of the transition zone. *Review of Geophysics*, *38*(1), 141–158.

Hirschmann, M., & Kohlstedt, D. (2012). Water in Earth's mantle. *Physics Today*, *65*(3), 40. https://doi.org/10.1063/PT.3.1476

Hsieh, W.-P. (2015). Thermal conductivity of methanol-ethanol mixture and silicone oil at high pressures. *Journal of Applied Physics*, *117*(23), 235901. https://doi.org/10.1063/1.4922632

Hsieh, W.-P. (2021). High-pressure thermal conductivity and compressional velocity of NaCl in B1 and B2 phase. *Scientific Reports*, *11*, 21321. https://doi.org/10.1038/s41598-021-00736-2

Hsieh, W. P., Chen, B., Li, J., Keblinski, P., & Cahill, D. G. (2009). Pressure tuning of the thermal conductivity of the layered muscovite crystal. *Physical Review B*, *80*(18), 180302. https://doi.org/10.1103/PhysRevB.80.180302

Hsieh, W. P., Deschamps, F., Okuchi, T., & Lin, J. F. (2017). Reduced lattice thermal conductivity of Fe-bearing bridgmanite in Earth's deep mantle. *Journal of Geophysical Research: Solid Earth*, *122*(7), 4900–4917. https://doi.org/10.1002/2017JB014339

Hsieh, W.-P., Deschamps, F., Okuchi, T., & Lin, J.-F. (2018). Effects of iron on the lattice thermal conductivity of Earth's deep mantle and implications for mantle dynamics. *Proceedings of the National Academy of Sciences of the United States of America*, *115*, 4099–4104. https://doi.org/10.1073/pnas.1718557115

Hsieh, W. P., Goncharov, A. F., Labrosse, S., Holtgrewe, N., Lobanov, S. S., Chuvashova, I., et al. (2020b). Low thermal conductivity of iron-silicon alloys at Earth's core conditions with implications for the geodynamo. *Nature Communications*, *11*, 3332. https://doi.org/10.1038/s41467-020-17106-7

Hsieh, W.-P., Ishii, T., Chao, K. H., Tsuchiya, J., Deschamps, F., & Ohtani, E. (2020a). Spin transition of iron in δ-(Al, Fe)OOH induces thermal anomalies in Earth's lower mantle. *Geophysical Research Letters*, *47*, e2020GL087036. https://doi.org/10.1029/2020GL087036

Hsieh, W.-P., Marzotto, E., Tsao, Y. C., Okuchi, T., & Lin, J.-F. (2022). High thermal conductivity of stishovite promotes rapid warming of a sinking slab in Earth's mantle. *Earth and Planetary Science Letters*, *584*, 117477. https://doi.org/10.1016/j.epsl.2022.117477

Irifune, T., & Ringwood, A. E. (1987). Phase transformations in a harzburgite composition to 26 GPa: Implications for dynamical behaviour of the subducting slab. *Earth and Planetary Science Letters*, *86*, 365–376. https://doi.org/10.1016/0012-821x(87)90233-0

Ishii, T., & Ohtani, E. (2021). Dry metastable olivine and slab deformation in a wet subducting slab. *Nature Geoscience*, *14*(7), 526–530. https://doi.org/10.1038/s41561-021-00756-7

Ishii, T., Ohtani, E., & Shatskiy, A. (2022). Aluminum and hydrogen partitioning between bridgmanite and high-pressure hydrous phases: Implications for water storage in the lower mantle. *Earth and Planetary Science Letters*, *583*, 117441. https://doi.org/10.1016/j.epsl.2022.117441

Jacobsen, S. D. (2006). Effect of water on the equation of state of nominally anhydrous minerals. *Reviews in Mineralogy and Geochemistry*, *62*, 321–342. https://doi.org/10.2138/rmg.2006.62.14

John, T., Scambelluri, M., Frische, M., Barnes, J. D., & Bach, W. (2011). Dehydration of subducting serpentinite: Implications for halogen mobility in subduction zones and the deep halogen cycle. *Earth and Planetary Science Letters*, *308*(1–2), 65–76. https://doi.org/10.1016/j.epsl.2011.05.038

Kang, K., Koh, Y. K., Chiritescu, C., Zheng, X., & Cahill, D. G. (2008). Two-tint pump-probe measurements using a femtosecond laser oscillator and sharp-edged optical filters. *Review of Scientific Instruments*, *79*(11), 114901. https://doi.org/10.1063/1.3020759

Katsura, T., & Ito, E. (1989). The system Mg2SiO4-Fe2SiO4 at high pressures and temperatures' precise determination of Stabilities of olivine, modified Spinel, and Spinel. *Journal of Geophysical Research*, *94*(89), 15663. https://doi.org/10.1029/jb094ib11p15663

Katsura, T., Yamada, H., Nishikawa, O., Song, M., Kubo, A., Shinmei, T., et al. (2004). Olivine-wadsleyite transition in the system (Mg, Fe)2SiO4. *Journal of Geophysical Research*, *109*, B02209. https://doi.org/10.1029/2003JB002438

Katsura, T., Yoneda, A., Yamazaki, D., Yoshino, T., Ito, E., Suetsugu, D., et al. (2010). Adiabatic temperature profile in the mantle. *Physics of the Earth and Planetary Interiors*, *183*(1–2), 212–218. https://doi.org/10.1016/j.pepi.2010.07.001

Kubo, T., Ohtani, E., Kato, T., Shinmei, T., & Fujino, K. (1998). Effects of water on the a-b transformation kinetics in san carlos olivine. *Science*, *281*, 85–87. https://doi.org/10.1126/science.281.5373.85

Lai, X., Zhu, F., Zhang, J. S., Zhang, D., Tkachev, S., Prakapenka, V. B., & Chen, B. (2020). An externally-heated diamond anvil cell for synthesis and single-crystal elasticity determination of Ice-VII at high pressure-temperature conditions. *Journal of Visualized Experiments*, *160*, e61389. https://doi.org/10.3791/61389

Litasov, K. D., Ohtani, E., Nishihara, Y., Suzuki, A., & Funakoshi, K. (2008). Thermal equation of state of Al- and Fe-bearing phase D. *Journal of Geophysical Research*, *113*(8), B08205. https://doi.org/10.1029/2007JB004937

Litasov, K. D., Ohtani, E., Suzuki, A., & Funakoshi, K. (2007). The compressibility of Fe- and Al-bearing phase D to 30 GPa. *Physics and Chemistry of Minerals*, *34*(3), 159–167. https://doi.org/10.1007/s00269-006-0136-4

Liu, L. (1986). Phase transformations in serpentine at high pressures and temperatures and implications for subducting lithosphere. *Physics of the Earth and Planetary Interiors*, *42*(4), 255–262. https://doi.org/10.1016/0031-9201(86)90028-2

Liu, L. (1987). Effects of H2O on the phase behaviour of the forsterite-enstatite system at high pressures and temperatures and implications for the Earth. *Physics of the Earth and Planetary Interiors*, *49*(1–2), 142–167. https://doi.org/10.1016/0031-9201(87)90138-5

Liu, X., Matsukage, K. N., Nishihara, Y., Suzuki, T., & Takahashi, E. (2019). Stability of the hydrous phases of Al-rich phase D and Al-rich phase H in deep subducted oceanic crust. *American Mineralogist*, *104*(1), 64–72. https://doi.org/10.2138/am-2019-6559

Mainprice, D., Le Page, Y., Rodgers, J., & Jouanna, P. (2007). Predicted elastic properties of the hydrous D phase at mantle pressures: Implications for the anisotropy of subducted slabs near 670-km discontinuity and in the lower mantle. *Earth and Planetary Science Letters*, *259*(3–4), 283–296. https://doi.org/10.1016/j.epsl.2007.04.053

Marquardt, H., & Thomson, A. R. (2020). Experimental elasticity of Earth's deep mantle. *Nature Reviews Earth & Environment*, *1*, 455–469. https://doi.org/10.1038/s43017-020-0077-3

Marzotto, E., Hsieh, W. P., Ishii, T., Chao, K. H., Golabek, G. J., Thielmann, M., & Ohtani, E. (2020). Effect of water on lattice thermal conductivity of ringwoodite and its implications for the thermal evolution of descending slabs. *Geophysical Research Letters*, *47*, e2020GL087607. https://doi.org/10.1029/2020GL087607

Meier, T., Aslandukova, A., Trybel, F., Laniel, D., Ishii, T., Khandarkhaeva, S., et al. (2021). In situ high-pressure nuclear magnetic resonance crystallography in one and two dimensions. *Matter and Radiation at Extremes*, *6*, 068402. https://doi.org/10.1063/5.0065879

Monkhorst, H. J., & Pack, J. D. (1976). Special points for Brillonin-zone integrations. *Physical Review B*, *13*, 5188–5192. https://doi.org/10.1103/physrevb.13.5188

Nestola, F., & Smyth, J. R. (2016). Diamonds and water in the deep Earth: A new scenario. *International Geology Review*, *58*(3), 263. https://doi.org/10.1080/00206814.2015.1056758

Nishi, M., Irifune, T., Tsuchiya, J., Tange, Y., Nishihara, Y., Fujino, K., & Higo, Y. (2014). Stability of hydrous silicate at high pressures and water transport to the deep lower mantle. *Nature Geoscience*, *7*(3), 224–227. https://doi.org/10.1038/ngeo2074

O'Hara, K. E., Hu, X., & Cahill, D. G. (2001). Characterization of nanostructured metal films by picosecond acoustics and interferometry. *Journal of Applied Physics*, *90*(9), 4852. https://doi.org/10.1063/1.1406543

Ohta, K., Yagi, T., Hirose, K., & Ohishi, Y. (2017). Thermal conductivity of ferropericlase in the Earth's lower mantle. *Earth and Planetary Science Letters*, *465*, 29–37. https://doi.org/10.1016/j.epsl.2017.02.030

Ohta, K., Yagi, T., Taketoshi, N., Hirose, K., Komabayashi, T., Baba, T., et al. (2012). Lattice thermal conductivity of MgSiO3 perovskite and post-perovskite at the core–mantle boundary. *Earth and Planetary Science Letters*, *349*(350), 109–115. https://doi.org/10.1016/j.epsl.2012.06.043

Ohtani, E. (2020). The role of water in Earth's mantle. *National Science Review*, *7*, 224–232. https://doi.org/10.1093/nsr/nwz071

Ohtani, E., Yuan, L., Ohira, I., Shatskiy, A., & Litasov, K. (2018). Fate of water transported into the deep mantle by slab subduction. *Journal of Asian Earth Sciences*, *167*, 2–10. https://doi.org/10.1016/j.jseaes.2018.04.024

Okuda, Y., Ohta, K., Sinmyo, R., Hirose, K., Yagi, T., & Ohishi, Y. (2019). Effect of spin transition of iron on the thermal conductivity of (Fe, Al)-bearing bridgmanite. *Earth and Planetary Science Letters*, *520*, 188–198. https://doi.org/10.1016/j.epsl.2019.05.042

Perdew, J., Burke, K., & Ernzerhof, M. (1996). Generalized gradient approximation made simple. *Physical Review Letters*, *77*(18), 3865–3868. https://doi.org/10.1103/PhysRevLett.77.3865

Peslier, A. H., Schönbächler, M., Busemann, H., & Karato, S. (2017). Water in the Earth' s interior: Distribution and origin. *Space Science Reviews*, *212*, 743–810. https://doi.org/10.1007/s11214-017-0387-z

Rosa, A. D., Sanchez-Valle, C., & Ghosh, S. (2012). Elasticity of phase D and implication for the degree of hydration of deep subducted slabs. *Geophysical Research Letters*, *39*(6), 6–11. https://doi.org/10.1029/2012GL050927

Sanchez-Valle, C., Sinogeikin, S. V., Smyth, J. R., & Bass, J. D. (2008). Sound velocities and elasticity of DHMS phase A to high pressure and implications for seismic velocities and anisotropy in subducted slabs. *Physics of the Earth and Planetary Interiors*, *170*(3–4), 229–239. https://doi.org/10.1016/j.pepi.2008.07.015

Satta, N., Marquardt, H., Kurnosov, A., Buchen, J., Kawazoe, T., McCammon, C., & Ballaran, T. B. (2019). Single-crystal elasticity of iron-bearing phase e and seismic detection of water in Earth's upper mantle. *American Mineralogist*, *104*(10), 1526–1529. https://doi.org/10.2138/am-2019-7084

Schmandt, B., Jacobsen, S. D., Becker, T. W., Liu, Z., Dueker, K. G., & Stamper-Kurn, D. M. (2014). Dehydration melting at the top of the lower mantle. *Science*, *344*, 1265–1489. https://doi.org/10.1126/science.1249850

Schmidt, A., Chiesa, M., Chen, X., & Chen, G. (2008). An optical pump-probe technique for measuring the thermal conductivity of liquids. *Review of Scientific Instruments*, *79*(6), 064902. https://doi.org/10.1063/1.2937458

Shieh, S. R., Mao, H. K., Hemley, R. J., & Ming, L. C. (1998). Decomposition of phase D in the lower mantle and the fate of dense hydrous silicates in subducting slabs. *Earth and Planetary Science Letters*, *159*(1–2), 13–23. https://doi.org/10.1016/S0012-821X(98)00062-4

Shieh, S. R., Mao, H. K., Konzett, J., & Hemley, R. J. (2000). In-situ high pressure X-ray diffraction of phase E to 15 GPa. *American Mineralogist*, *85*(5–6), 765–769. https://doi.org/10.2138/am-2000-5-616

Stein, C. A., & Stein, S. (1992). A model for the global variation in oceanic depth and heat flow with lithospheric age. *Nature*, *359*, 123–129. https://doi.org/10.1038/359123a0

Suzuki, A., Ohtani, E., Morishima, H., Kubo, T., Kanbe, Y., Kondo, T., et al. (2000). In situ determination of the phase boundary between wadsleyite and ringwoodite in Mg2SiO4. *Geophysical Research Letters*, *27*(6), 803–806.

Syracuse, E. M., Keken, P. E. V., & Abers, G. A. (2010). The global range of subduction zone thermal models. *Physics of the Earth and Planetary Interiors*, *183*, 73–90. https://doi.org/10.1016/j.pepi.2010.02.004

Tsuchiya, J., & Tsuchiya, T. (2008). Elastic properties of phase D (MgSi2O6H2) under pressure: Ab initio investigation. *Physics of the Earth and Planetary Interiors*, *170*(3–4), 215–220. https://doi.org/10.1016/j.pepi.2008.05.015

Tsuchiya, J., Tsuchiya, T., & Tsuneyuki, S. (2005). First-principles study of hydrogen bond symmetrization of phase D under high pressure. *American Mineralogist*, *90*(1), 44–49. https://doi.org/10.2138/am.2005.1628

Turcotte, D. L., & Schubert, G. (2014). *Geodynamics*. Cambridge University Press. https://doi.org/10.1017/CBO9780511843877

van Mierlo, W. L., Langenhorst, F., Frost, D. J., & Rubie, D. C. (2013). Stagnation of subducting slabs in the transition zone due to slow diffusion in majoritic garnet. *Nature Geoscience*, *6*, 400–403. https://doi.org/10.1038/ngeo1772

Wei, S. S., Wiens, D. A., van Keken, P. E., & Cai, C. (2017). Slab temperature controls on the Tonga double seismic zone and slab mantle dehydration. *Science Advances*, *3*, e1601755. https://doi.org/10.1126/sciadv.1601755

Wu, X., Wu, Y., Lin, J.-F., Liu, J., Mao, Z., Guo, X., et al. (2016). Two-stage spin transition of iron in FeAl-bearing phase D at lower mantle. *Journal of Geophysical Research: Solid Earth*, *121*, 6411–6420. https://doi.org/10.1002/2015JB012608.Received

Xu, C., & Inoue, T. (2019). Melting of Al-rich phase D up to the uppermost lower mantle and transportation of H2O to the deep Earth. *Geochemistry, Geophysics, Geosystems*, *20*(9), 4382–4389. https://doi.org/10.1029/2019GC008476

Xu, Y., Shankland, T. J., Linhardt, S., Rubie, D. C., Langenhorst, F., & Klasinski, K. (2004). Thermal diffusivity and conductivity of olivine, wadsleyite and ringwoodite to 20 GPa and 1373 K. *Physics of the Earth and Planetary Interiors*, *143*, 321–336. https://doi.org/10.1016/j.pepi.2004.03.005

Yang, D., Wang, W., & Wu, Z. (2017). Elasticity of superhydrous phase B at the mantle temperatures and pressures: Implications for 800 km discontinuity and water flow into the lower mantle. *Journal of Geophysical Research: Solid Earth*, *122*(7), 5026–5037. https://doi.org/10.1002/2017JB014319

Yang, H., Prewitt, C. T., & Frost, D. J. (1997). Crystal structure of the dense hydrous magnesium silicate, phase D. *American Mineralogist*, *82*(5–6), 651–654. https://doi.org/10.2138/am-1997-5-627

Zhan, Z. (2020). Mechanisms and implications of deep earthquakes. *Annual Review of Earth and Planetary Sciences*, *48*, 147–174. https://doi.org/10.1146/annurev-earth-053018-060314

Zhang, Y., Yoshino, T., Yoneda, A., & Osako, M. (2019). Effect of iron content on thermal conductivity of olivine with implications for cooling history of rocky planets. *Earth and Planetary Science Letters*, *519*, 109–119. https://doi.org/10.1016/j.epsl.2019.04.048

Zheng, X., Cahill, D. G., Krasnochtchekov, P., Averback, R. S., & Zhao, J. C. (2007). High-throughput thermal conductivity measurements of nickel solid solutions and the applicability of the Wiedemann-Franz law. *Acta Materialia*, *55*(15), 5177–5185. https://doi.org/10.1016/j.actamat.2007.05.037